Theoretical investigation of nitrogen-vacancy defects in silicon

Potsidi, M., Kuganathan, K., Christopoulos, S., Sarlis, N. V., Chroneos, A. & Londos, C. A

DOI 10.1063/5.0075799
ESSN 2158-3226

Publisher: American Institute of Physics

Theoretical investigation of nitrogen-vacancy defects in silicon

Cite as: AIP Advances **12**, 025112 (2022); https://doi.org/10.1063/5.0075799
Submitted: 18 October 2021 • Accepted: 18 January 2022 • Published Online: 07 February 2022

M. S. Potsidi, N. Kuganathan, S.-R. G. Christopoulos, et al.

Theoretical investigation of nitrogen-vacancy defects in silicon

Cite as: AIP Advances 12, 025112 (2022); doi: 10.1063/5.0075799
Submitted: 18 October 2021 • Accepted: 18 January 2022 •
Published Online: 7 February 2022

M. S. Potsidi,[1] N. Kuganathan,[2,3,a)] S.-R. G. Christopoulos,[2] N. V. Sarlis,[1] A. Chroneos,[2,4] and C. A. Londos[1]

AFFILIATIONS

[1] Section of Condensed Matter Physics, Department of Physics, National and Kapodistrian University of Athens, Panepistimiopolis Zografos, Athens 157 84, Greece
[2] Faculty of Engineering, Environment and Computing, Coventry University, Priory Street, Coventry CV1 5FB, United Kingdom
[3] Department of Materials, Imperial College, London SW7 2AZ, United Kingdom
[4] Department of Electrical and Computer Engineering, University of Thessaly, 38221 Volos, Greece

[a)] **Author to whom correspondence should be addressed:** n.kuganathan@imperial.ac.uk

ABSTRACT

Nitrogen-vacancy defects are important for the material properties of silicon and for the performance of silicon-based devices. Here, we employ spin polarized density functional theory to calculate the minimum energy structures of the vacancy-nitrogen substitutional, vacancy-dinitrogen substitutionals, and divacancy-dinitrogen substitutionals. The present simulation technique enabled us to gain insight into the defect structures and charge distribution around the doped N atom and the nearest neighboring Si atoms. Using the dipole–dipole interaction method, we predict the local vibration mode frequencies of the defects and discuss the results with the available experimental data.

I. INTRODUCTION

Defects are present in silicon mainly because of crystal growth and processing conditions.[1,2] These can impact the material properties of silicon and consequently the performance of devices. In addition, the improvement in physical properties through the introduction of dopants is common in semiconductors.[1,2]

Here, we focus on nitrogen (N), which is important for processing devices, as it can lock dislocations and consequently increase the mechanical strength of wafers.[3] In turn, this is significant for the very large scale integration (VLSI) and ultra-large-scale integration (ULSI) technologies of Si as it permits the Si wafer to undergo a range of processing steps without breaking. In practical terms, the introduction of N results in larger wafers with improved mechanical stability and wafer flatness. The positive impact of N includes the suppression of the negative effect of metal contaminants[4] and the reduction in voids and microdefects (for example, A-swirls and D-defects) during float-zone crystal growth.[5,6] Importantly, the interaction of N with oxygen-related defects affects the formation of thermal donors in Si, influencing the electrical properties of Czochralski grown Si.[7] It is also beneficial as it prevents the formation of A-centers[8] and enhances oxygen precipitate formation.[9] To summarize, N influences the mechanical, optical, and electrical properties of Si.[10]

Under equilibrium conditions, the solid solubility of N in Si is low ($4.5–10 \times 10^{15}$ atoms/cm^3 near the melting point) compared to that of O and C that are common impurities in Si.[11] Typically, N interacts with self-interstitials, C and O, but the interaction with vacancies is limited as their concentration is less.[11] Nevertheless, when considering non-equilibrium conditions (such as irradiation), there can be a supersaturation of vacancies that can lead to a significant concentration of nitrogen-vacancy defects. Here, we focus on the nitrogen-vacancies as there are still undetermined issues regarding their structure and properties, irrespective of the significantly available literature.[12–16]

In the present study, we employ density functional theory (DFT) to study the structure and properties of the vacancy-nitrogen substitutional, vacancy-dinitrogen substitutional, and divacancy-dinitrogen substitutional defects in Si. For the minimum energy structures, we employ the dipole–dipole interaction method to

predict the local vibration mode (LVM) frequencies of these defects.

II. METHODOLOGY

We used a DFT code VASP (Vienna *Ab* initio Simulation Package)[17] to perform all calculations. This code uses plane wave basis sets and projected augmented wave (PAW) pseudopotentials[18] to solve standard Kohn–Sham equations. A plane wave basis set with a cut-off of 500 eV was used in all calculations. 8 × 8 × 8 and 4 × 4 × 4 Monkhorst–Pack[19] *k*-point meshes were used to model bulk Si and defect structures, respectively. Only a small difference in total energy (0.6 meV) was observed with further increasing k-points. All defect calculations were performed using a supercell containing 250 atoms. The generalized gradient approximation (GGA) as parameterized by Perdew, Burke, and Ernzerhof (PBE)[20] was used to describe the exchange-correlation energy. Full geometry optimization (both atom positions and lattice constants were relaxed simultaneously) calculations were performed with an aid of the conjugate gradient algorithm.[21] We performed single point calculations on the pre-relaxed defect configurations using the hybrid Heyd–Scuseria–Ernzerhof (HSE) functional[22] and then plotted densities of states (DOSs) to see impurity states clearly. The screening parameter (HFSCREEN) used in this study is 0.20. The fractions of exchange and gradient correction were set to 0.25 and 0.75, respectively. Forces on the atoms and stress tensor were less than 0.001 eV/Å and 0.002 GPa, respectively, in all relaxed configurations. All calculations were performed in the absence of symmetry. Spin polarization was introduced in all calculations. Bader charge analysis[23] was carried out to estimate the charges on the doped atoms. The Bader charge analysis is an effective tool to estimate the electronic charges on the atoms in the lattice. In this method, zero flux surfaces are used to divide atoms and partition the charge density. The following equation was used to express the zero flux surface of the gradients of the electron density as defined by Yu and Trinkle:[24]

$$\nabla\rho(\vec{r})\hat{n} = 0, \tag{1}$$

where $\rho(\vec{r})$ is the electron density and $\hat{n}$ is the unit vector perpendicular to the dividing surface at any surface point $(\vec{r})$.

Short range dispersive attraction was included in the form of semi-empirical force field as implemented by Grimme *et al.*[25]

III. RESULTS AND DISCUSSION

A. DFT calculations

1. Crystal structure

In order to validate the quality of the basis sets and pseudopotentials used in this study, we performed a series of single point calculations on the crystal structure of cubic Si (space group $Fd\bar{3}m$, No : 227)[26] as shown in Fig. 1(a) to obtain the equilibrium lattice constants and bulk modulus (see Table I). The lattice constants were allowed to vary within ±5% of the equilibrium lattice constant value. Figure 1(b) shows the energy vs lattice constant curve plotted by fitting the calculated energies in the Murnaghan equation of state.[27] The calculated equilibrium lattice constant (5.45 Å) and bulk modulus (0.87 Mbar) were in good agreement with previous experimental[26,28] and the other theoretical values,[28–30] showing the efficacy of the pseudopotentials and basis sets (refer to Table I). Cohesive energy was calculated using the following equation:

$$E_{coh}(Si) = E_{Si}^{isolated} - E_{Si}^{bulk}, \tag{2}$$

where $E_{Si}^{isolated}$ and E_{Si}^{bulk} are the total energies of an isolated gas phase Si atom and a Si atom in the bulk, respectively. There is good agreement between the calculated (4.73 eV/atom) and experimental

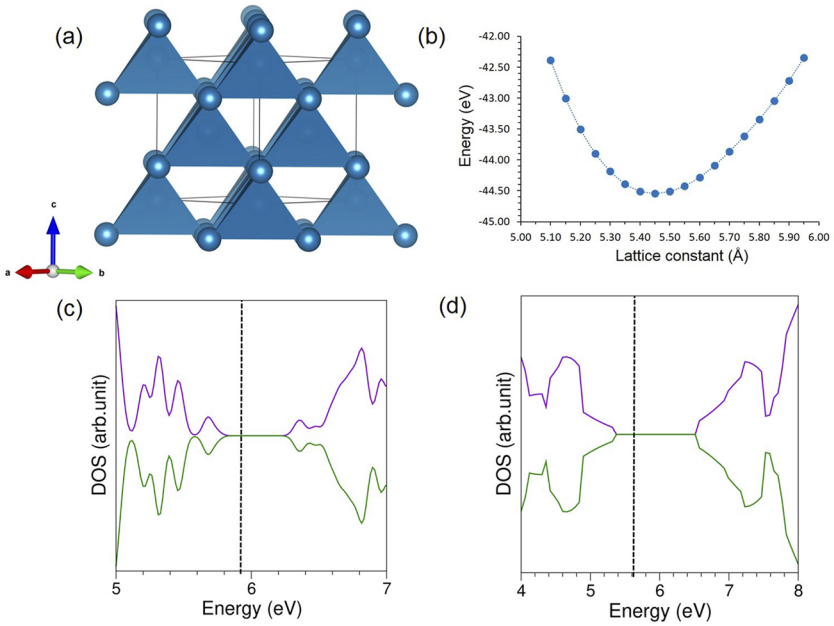

FIG. 1. (a) Relaxed structure of Si bulk, (b) plot of total energy vs lattice constant and (c) and (d) DOS plots calculated for the bulk Si using GGA and HSE functionals, respectively. Vertical black dot lines correspond to the Fermi energy level.

TABLE I. Calculated lattice parameter, bulk modulus, cohesive energy, and bandgap. Corresponding experimental values are also provided.

Parameter	This study	Experiment	Other calculation
a = b = c (Å)	5.45	5.43[26]	5.42,[29] 5.46[30]
B*o* (Mbar)	0.87	0.99[28]	0.89,[30] 0.92,[30] 0.96,[30] 0.98[28]
E_{coh} (eV/atom)	4.73	4.63[28]	4.84,[28] 5.10[31]
E_{gap} (eV)	0.65, 1.15	1.17[32]	0.60,[33] 0.61,[34] 0.71,[34] 1.11[34]

(4.63 eV/atom) values.[28] The cohesive energies calculated in other DFT simulations are slightly overestimated from this study and the experiment.[28,31] The calculated density of states (DOS) of the bulk Si is shown in Fig. 1(c). The calculation reveals that bulk Si is a semiconductor with a bandgap of ~0.65 eV, which is in reasonable agreement with an experimental value of 1.17 eV[32] and good agreement with the values obtained from other DFT calculations.[32,33] The underestimation of bandgap is very common in GGA-PBE calculations.[34] Hybrid functionals can provide a good bandgap prediction although calculations are computationally expensive.[35,36] We performed single point calculation on the pre-relaxed configuration of bulk Si using HSE functional, and then DOS calculation was performed. The bandgap value was estimated to be ~1.15 eV, which is in good agreement with the experimental value of 1.17 eV.[32]

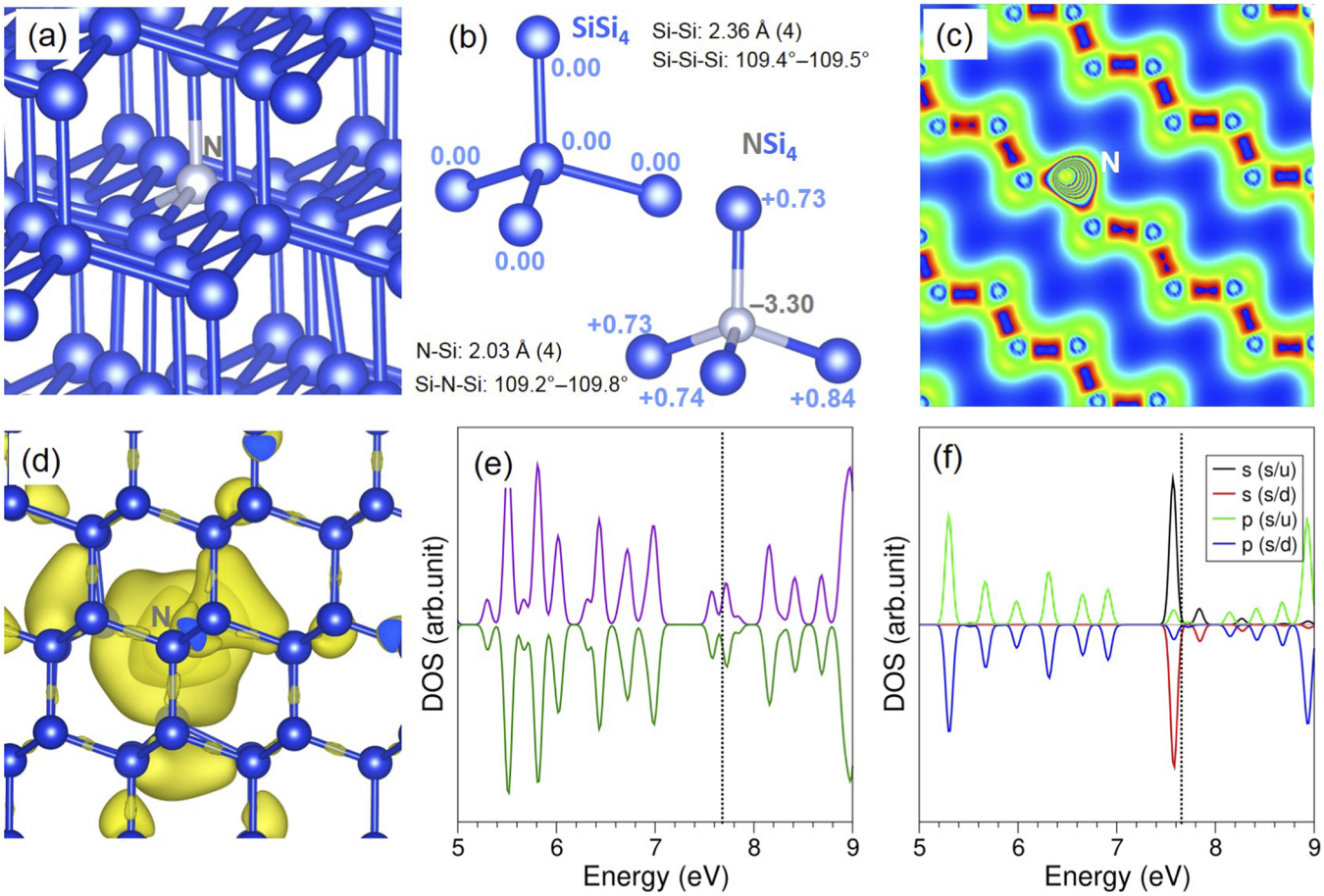

FIG. 2. (a) Relaxed structure of N-substituted Si, (b) tetrahedral units showing bond distances, bond angles, and the Bader charges in the relaxed configurations of Si and N-substituted Si, (c) charge density plot showing the bonding interaction of N, (d) band-decomposed charge density plot associated with the N, (e) total DOS plot, and (f) atomic DOS plot of N.

2. Nitrogen doped Si

A single N atom was substitutionally doped on the Si site. The relaxed structure shows that the N atom forms a tetragonal unit (NSi_4) with almost identical bond angles (Si–N–Si) compared to the Si–Si–Si bond angles of the $SiSi_4$ unit in the bulk Si. The N–Si bond lengths are shorter (by ~0.3 Å) than the Si–Si bond lengths [see Figs. 2(a) and 2(b)]. The bond-lengths, bond-angles, and Bader chargers were compared with those calculated using fixed volume relaxations. The results demonstrate that lattice constants and lattice angles of the defect supercells did not deviate from the ideal supercell considerably (see Fig. S1 in the electronic supplementary material). The bonding interaction between the N and the Si is shown by plotting a charge density map [see Fig. 2(c)]. The strong bonding nature is evidenced by the shorter N–Si bond lengths. This is further confirmed by the negative Bader charge on the N atom and the positive Bader charges on the Si in the NSi_4 tetrahedral unit. According to the Bader charge analysis, the N atom gains approximately three electrons from the nearest neighbor Si atoms [see Fig. 2(b)]. This is due to the higher electronegativity of N (3.04) than Si (1.90).[37] The substitution of N leaves approximately three positive charges in the lattice, and they are almost equally distributed on the four nearest neighboring Si atoms [see Fig. 2(b)]. The presence of electron density on the N is shown in Fig. 2(d). The states appearing in the bandgap are mainly associated with s electrons of N. The *p*-states of N are strongly localized with the lattice as these states are in the valence band [see Figs. 2(e) and 2(f)].

Substitution energy for a single nitrogen atom to replace a single Si atom was calculated using the following equation:

$$E_{Sub} = E_{(N:Si\_supercell)} + E_{(Si)} - E_{(Si\_supercell)} - \frac{1}{2}E(N_2), \quad (3)$$

where $E_{(N:Si\_supercell)}$ is the total energy of a single N atom substitutionally doped in the Si supercell, $E_{(Si\_supercell)}$ is the total energy of the defect free Si supercell, $E_{(Si)}$ is the energy of a Si atom in the

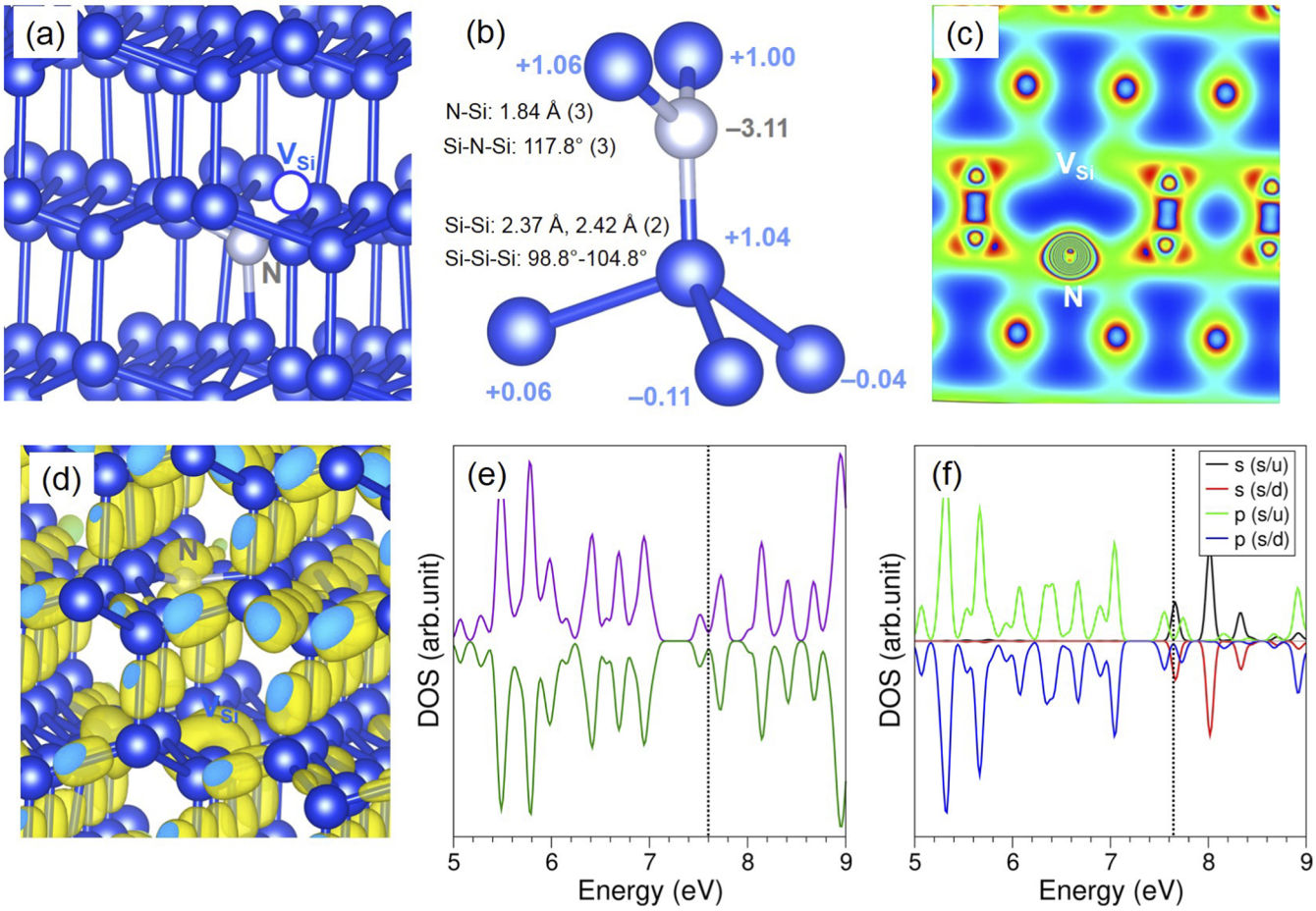

FIG. 3. (a) Relaxed structure of a single N atom substitutionally doped on the Si site in the presence of a Si vacancy closer to the dopant, (b) a structural unit showing bond distances, bond angles, and Bader charges around the dopant, (c) charge density plot associated with the *V*N pair, (d) band-decomposed charge density plot around the N atom, (e) total DOS plot of N-doped Si structure, and (f) atomic DOS plot of N.

bulk Si, and $E(N_2)$ is the total energy of a N_2 molecule. Substitution energy is endothermic (0.50 eV), inferring the strong Si–Si bond in the bulk Si. However, the doping process can be practically possible at moderate temperatures.

The energy to incorporate single N atoms on the pre-existing Si vacancy defect was calculated according to the following equation:

$$E_{Inc} = E_{(N:Si\_supercell)} - E_{V_{Si}:supercell} - \frac{1}{2}E(N_2), \quad (4)$$

where $E_{V_{Si}:supercell}$ is the total energy of the supercell consisting of a Si vacancy. The incorporation energy is −3.01 eV, suggesting that the N prefers to occupy the vacancy site if there is a vacancy readily available.

3. The vacancy-nitrogen substitutional defect

Next, we performed a calculation on a single N atom doped on the Si site closer to a pre-existing Si vacancy. Si vacancy formation energy was calculated in the absence of N doping. The Si vacancy formation energy is 3.51 eV, agreeing well with previous calculation.[38]

We have considered different vacancy-nitrogen substitutional defect configurations (see Fig. S3 in the supplementary material), and the lowest energy structure is shown in Fig. 3(a). The doped N atom forms a distorted trigonal planar structure with three identical bond angles of 117.8° and three Si–N bond lengths of 1.84 Å. Formation of this three coordinated structure is due to the presence of a nearest neighbor Si vacancy. The presence of the Si vacancy significantly changes the Si–N bond distances compared to those calculated in the absence of Si vacancy [see Figs. 2(b) and (3b)]. A significant reduction of ~0.20 Å in the N–Si bond distances is noted. This is due to the strong bonding between the N and Si atoms as confirmed by the higher positive Bader charges (~+1.00) on the Si atoms than on the Si atoms (~+0.76), forming a tetrahedral unit with N atoms in the absence of Si vacancy. The Bader charge analysis shows that the N atom gains approximately three electrons from three Si atoms to which it bonded. In the NSi_4 tetrahedral unit, there is a slight difference in the bond lengths and significant perturbation in the bond angles compared to those calculated in the regular $SiSi_4$ of the bulk Si. The calculated bond-lengths, bond-angles, and Bader chargers

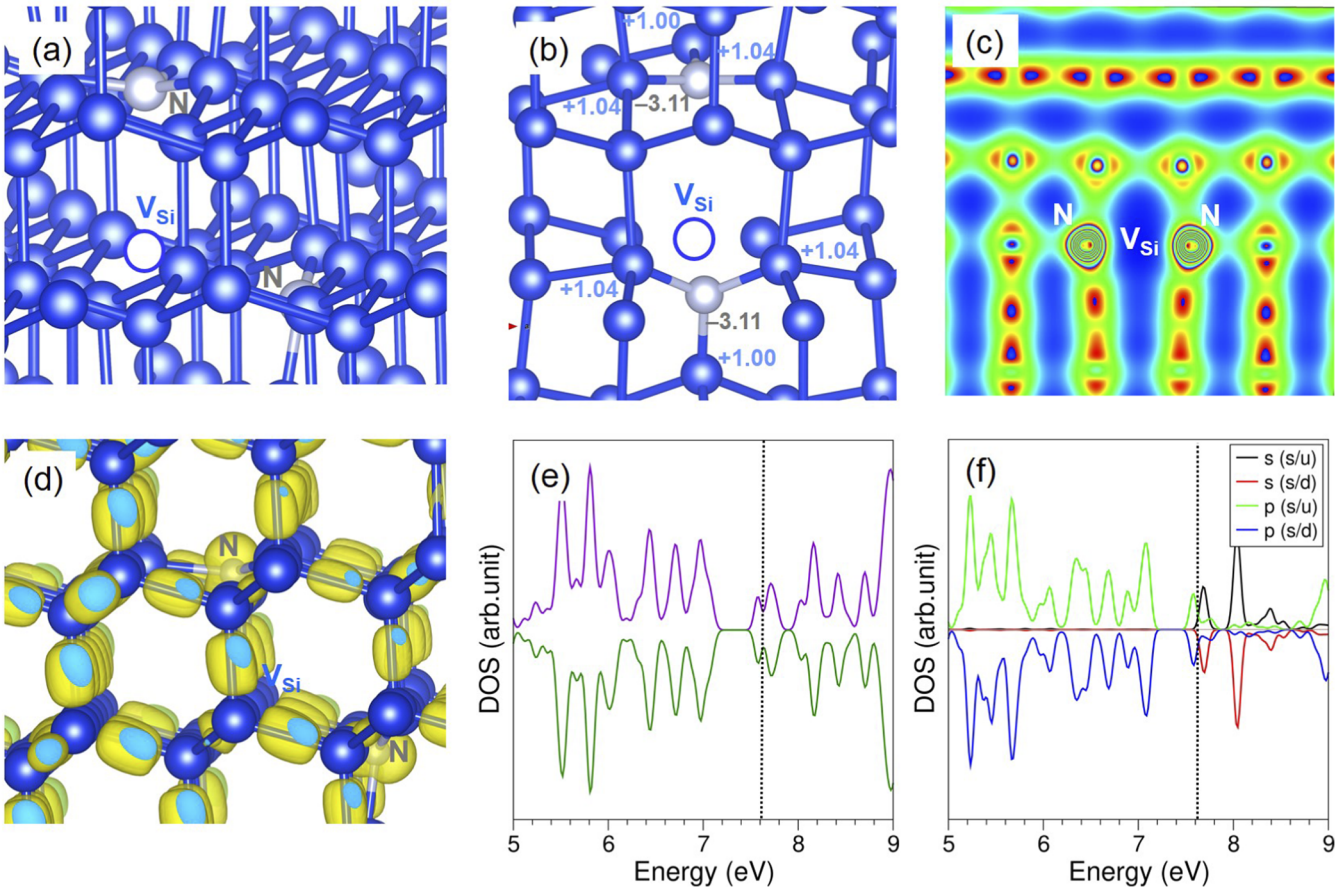

FIG. 4. (a) Relaxed structure of two N atoms substitutionally doped on the Si sites in the presence of a Si vacancy closer to the dopants, (b) a structural unit showing bond distances, bond angles, and Bader charges around the dopants, (c) charge density plot associated with the N–*V*–N cluster, (d) band-decomposed charge density plot around the N atoms, (e) total DOS plot of the doped Si, and (f) atomic DOS plot of N.

were not affected considerably compared to those calculated using fixed volume relaxations (see Fig. S2 in the supplementary material). The charge density plot shows the charge distribution around the defects and their locations [see Fig. 3(c)]. The localization of electrons around the doped N and the Si vacancy is shown in Fig. 3(d). The total DOS plot shows that the resultant doped structure is an *n*-doped band-gap material. The states appearing in the bandgap are mainly associated with *s* and *p* electrons of N [see Figs. 3(e) and 3(f)].

We calculated the vacancy formation energy of a Si atom in the absence and the presence of N doping. N doping facilitates the formation of a Si vacancy by 2.10 eV. Furthermore, we calculated the binding energy to form a *V*N cluster from isolated nitrogen and vacancy defects. The calculated binding energy is −2.10 eV, meaning that the cluster form is more stable than the isolated form.

4. The vacancy-dinitrogen substitutional defect

Two N atoms substitutionally doped on the Si sites were considered in the presence of a single nearest neighbor Si vacancy. We have considered different configurations (see Fig. S4 in the supplementary material), and the lowest energy structure is shown in Fig. 4(a). As discussed earlier, each N atom forms a three coordinated structure with three nearest neighbor Si atoms, and the N–Si bond lengths and bond angles are almost the same as the values calculated in the *V*N configuration [see Fig. 4(b)]. The Bader charge on each N atom is −3.11. The negative charge on the N is due to the loss of approximately one electron from each three Si atoms. The charge density plot associated with the doped N atoms together with a Si vacancy is shown in Fig. 4(c). The band-decomposed charge density plot around the N atom indicates that the electrons are mainly localized on the N atoms. The total DOS plot shows that the resultant doped configuration is still a semiconductor [see Fig. 4(e)]. The *p* states of N are mainly localized in the valence band [see Fig. 4(f)]. The binding energy to form the N–*V*–N cluster from isolated defects (2 N and *V*) is calculated to be −3.62 eV, inferring the preference of forming the cluster.

5. The divacancy-dinitrogen substitutional defect

Here, we discuss the structures and electronic structures of two N atoms substitutionally doped on the Si sites in the presence

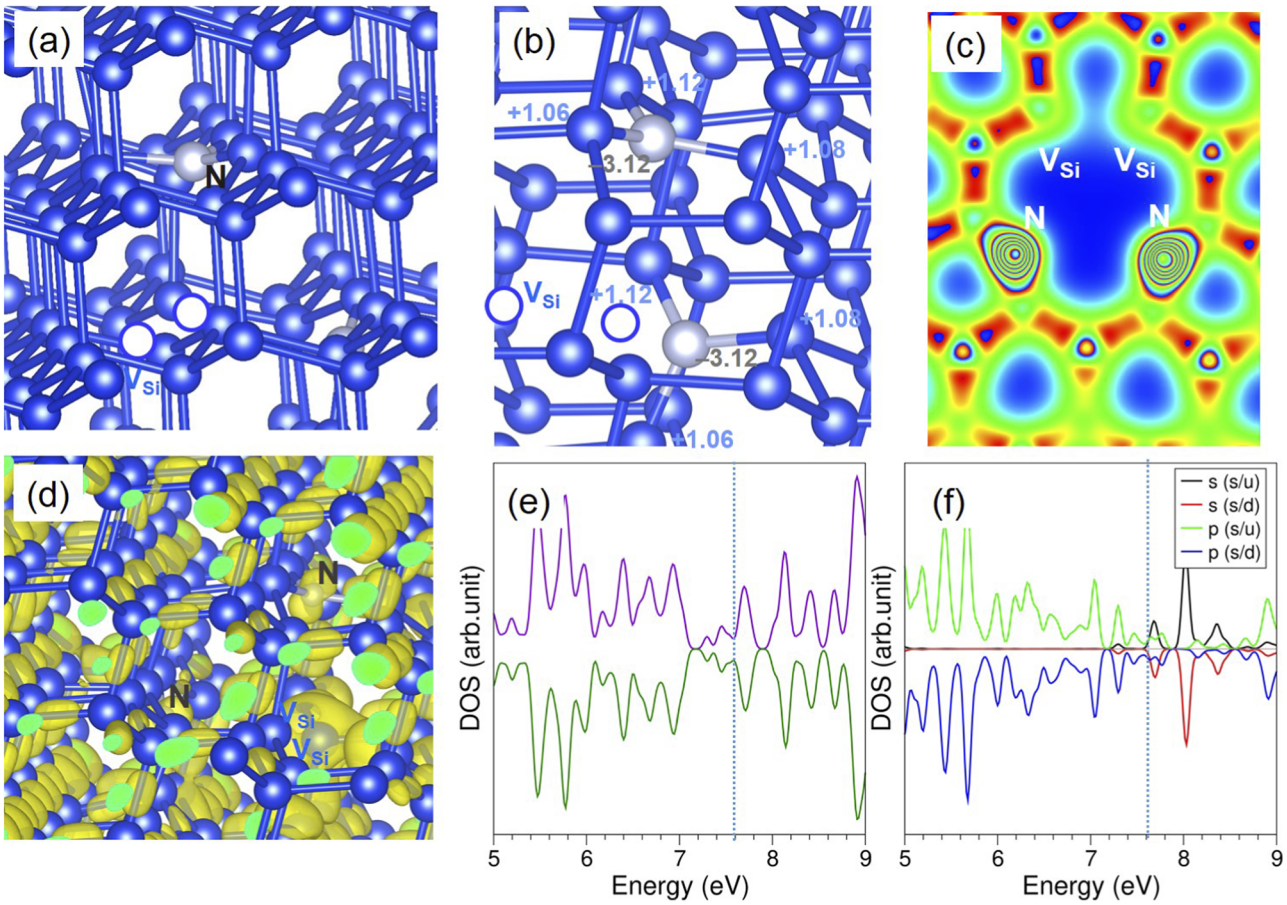

FIG. 5. (a) Relaxed configuration of N_{Si}–V_{Si}–V_{Si}–N_{Si} cluster, (b) a structural unit showing Bader charges around the N atom, (c) charge density plot showing the bonding interaction between the N and Si, (d) band-decomposed charge density plot around the N atoms, (e) total DOS plot of the doped configuration, and (f) atomic DOS plot of N.

TABLE II. Binding energies calculated for the formation of V_2N_2 cluster.

Defect cluster formation process	Binding energy (eV)
$VN + VN \rightarrow V_2N_2$	−0.79
$VN_2 + V \rightarrow V_2N_2$	−1.37
$2\,N + 2\,V \rightarrow V_2N_2$	−4.99

of two Si vacancies. We have considered different configurations (see Fig. S5 in the supplementary material), and the lowest energy structure is shown in Fig. 5(a). Negative Bader charge (−3.12) on each N is donated by the three Si atoms (~1.05*e* from each Si) [see Fig. 5(b)]. A distorted trigonal planar unit (NSi_3) is formed by the doped N and three Si atoms, as seen previously. Shorter N–Si bonds (1.84 Å) confirm the strong bonding nature between the N and Si. The cross-sectional charge density plot shows the bonding interaction between the N and Si in the NSi_3 unit [see Fig. 5(c)]. Electron density around the N atoms is shown in Fig. 5(d). The total DOS plot shows that the resultant structure introduces gap states [see Fig. 5(e)]. The atomic DOS plot of N is shown in Fig. 5(f). The Fermi energy level is localized with s and *p* states of N.

We calculated the binding energy for the formation of the V_2N_2 cluster via different routes (see Table II). For example, the binding energy of the V_2N_2 cluster from two *V*N defect clusters was calculated using the following equation:

$$E_{Binding}(V_2N_2) = E(V_2N_2) + E_{(Si\_supercell)} - 2E(NV), \quad (5)$$

where $E(V_2N_2)$ and $E(NV)$ are the total energies of the supercell consisting of V_2N_2 and NV defect clusters, respectively.

Binding energy is exothermic in all cases. The cluster formation from the isolated point defects (N and V) is highly exothermic (−4.99 eV) compared to the process consisting of sub-clusters (*V*N or VN_2). The energy to form a single Si vacancy from the defect free Si supercell and the supercell consisting of the VN_2 cluster was calculated. There is an enhancement in the formation of vacancy by 6.53 eV in the presence of the VN_2 cluster.

B. Dipole–dipole interaction method

1. The vacancy-nitrogen substitutional defect

The lowest energy configuration of the nitrogen substitutional-vacancy center (*V*N) defect as derived by our DFT calculations is displayed in Fig. 6. The Si vacancy resides in the nearest neighbor site with respect to the N substitutional. The defect includes a N atom at a substitutional lattice site, bonded to three silicon neighboring lattice atoms, with the fourth lattice site being vacant.

To calculate the vibrational mode frequencies of the *V*N defect, we have applied a previously used procedure, based on the comparison of the *V*N structure to similar molecular structures.[39] In our studies, the *V*N defect in silicon displays a C_{3v} symmetry configuration [Fig. 6(a)], also reported in the previous study by Platonenko *et al.*[16] This geometry is similar to the C_{3v} pyramidal geometry of triarsenic phosphide (As_3P), shown in Fig. 6(b).[40,41] The nitrogen atom in the *V*N defect bonds to three *Si* lattice atoms with all N–Si bonds being of equal length d_{N-Si} = 1.833 Å and the nitrogen-silicon mass ratio being equal to $\frac{m_N}{m_{Si}} = 0.5$. In the As_3P molecule, the phosphorus–arsenic mass ratio is $\frac{m_P}{m_{As}} = 0.4$, a value very close to the $\frac{m_N}{m_{Si}}$ value.

Moreover, every angle ∠Si–N–Si in the *VN* defect provided by our DFT results has a value of ~119°, which lies close to the ~109° angle ∠As–P–As value in the As_3P molecule.[40] In addition, in both *V*N and As_3P configurations, nitrogen and phosphorus atoms are *Group-V* elements in the Periodic Table, exhibiting the same valence electron orbital configuration, with valence electrons occupying *p* orbitals in both elements.

Based on all previous considerations, we may assume that the force constants of the modes of vibrating N and P atoms in the *V*N and As_3P configurations, respectively, are approximately the same. As a result, the vibrating frequencies of the N and P atoms, ω_{VN} and ω_{As_3P}, correspondingly relate through the formula

$$\omega_{VN} = \sqrt{\frac{m_P}{m_N}}\,\omega_{As_3P}, \quad (6)$$

where $m_P = 31\,amu$ and $m_N = 14\,amu$ are the atomic masses of P and N atoms, respectively. By substituting $\omega_{As_3P} = 450\ cm^{-1}$

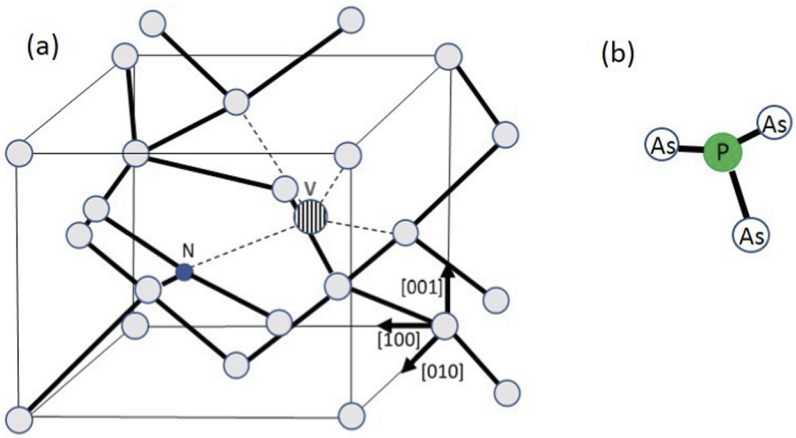

FIG. 6. (a) Lowest energy *V*N configuration in Si. The striped circle denotes the vacant site while blue and light gray circles denote substitutional nitrogen and Si atoms, respectively. (b) The As_3P C_{3v} configuration. Green and white circles are for phosphorus and arsenic atoms, respectively.

corresponding to the $\nu_1(\alpha_1)$ frequency of the As_3P,[40] we get ω_{VN} = 670cm^{-1}, a value located very close to the experimental frequency at 663[13] and 668 cm^{-1}[16] of the *VN* defect. In a previous theoretical study, Platonenko *et al.*[16] employed hybrid DFT and calculated a similar structure to the *V*N defect in the present study; however, their calculated band was at 654 cm^{-1}.

2. The vacancy-dinitrogen substitutional defect

To form the VN_2 defect, we introduce a further N atom at all possible sites near the *V*N defect. Figure 7(a) depicts the lowest energy configuration of the VN_2 defect as derived by DFT calculations. VN_2 consists of a *V*N defect (with the nitrogen atom denoted as N_A) joined by a second nitrogen substitutional atom (denoted as N_B) at a distance $d_{N_A-N_B}$ = 4.81 Å. The second nitrogen atom inserted in the vicinity of the *VN* defect also bonds to three Si neighbors forming a tetrahedral structure with geometrical parameters similar to those of *V*N defect. Therefore, the structure resembles two vacancy-nitrogen defects, with the two C_3 symmetry axes pointing toward the same vacancy. In all N–Si covalent bonds, in both vacancy-nitrogen pairs comprising the VN_2 defect, the overlapping orbitals of different N and Si atomic radii are expected to cause an imbalance in electron density and lead to a region of partial negative charge δ^- [Fig. 7(b)] closer to the smaller N atom.[42] This charge accumulation, combined with the symmetry criteria that the two *V*N pairs fulfill, leads to a total dipole moment $\boldsymbol{p}_t$ [Fig. 2(c)] fixed upon the nitrogen atom, in the direction of the C_3 axis.[42] This total dipole moment results from the contributions of the components of the three individual N–Si bonds in the C_3 axis, in both vacancy-nitrogen pairs of the VN_2 defect [refer to Fig. 7(c)].[42]

It is known that in a very approximate consideration,[42] the dipole moment of every N–Si bond could be taken equal to the electronegativity difference $\Delta\chi_{N-Si}$ of *N* and *Si* atoms, in Debye units. However, in this work, we have used a reported approximation for the calculation of the partial charge δ on the nitrogen atom[43] based on Pauling's formula.[44,45] Thus, the partial charge δ on the nitrogen atom could be given by the relation

$$\delta = \left[1 - e^{-0.25(\Delta\chi_{N-Si})^2}\right]|e|, \tag{7}$$

where $\Delta\chi_{N-Si} = \chi_N - \chi_{Si}$ = 1.15, with χ_N = 3.066 and χ_{Si} = 1.916 being the Allen scale electronegativity values of nitrogen and silicon, respectively,[46] and *e* is the electron charge. We finally compute the value $\delta = 0.282|e|$.

The two *V*N dipoles have total dipole moments $\boldsymbol{p}_{t,A}$ and $\boldsymbol{p}_{t,B}$, which are the resultants of the three components of the individual N–Si dipole moments, $\boldsymbol{p}$, in the nitrogen-vacancy direction. As seen in Fig. 7(c), in the two *V*N geometries, every N–Si bond creates a dipole moment $\boldsymbol{p} = \delta \cdot \boldsymbol{r}$, where δ is the charge fixed on the nitrogen atoms and $\boldsymbol{r}$ is the vector pointing from the Si to the N atom. Assuming the dipoles oscillate along the nitrogen-vacancy directions, which shall be noted as $\boldsymbol{q}_A$ and $\boldsymbol{q}_B$, the total dipole moments $\boldsymbol{p}_{t,A}$ and $\boldsymbol{p}_{t,B}$ are given by the relations

$$\boldsymbol{p}_{t,A} = 3 \cdot \delta \cdot \cos\theta \cdot (r + q_A)\hat{\boldsymbol{q}}_A, \quad \boldsymbol{p}_{t,B} = 3 \cdot \delta \cdot \cos\theta \cdot (r + q_B)\hat{\boldsymbol{q}}_B, \tag{8}$$

where *r* is the N–Si bond lengths, θ is half of the ∠Si–N–Si angles, q_A and q_B denote the displacements of the two vibrating nitrogen atoms along the $\boldsymbol{q}_A$ and $\boldsymbol{q}_B$ directions, respectively, and $\hat{\boldsymbol{q}}_A$ and $\hat{\boldsymbol{q}}_B$ are the corresponding unit vectors.

The calculation of the LVM frequencies of the VN_2 defect employs a previously used method,[47–50] based on the interaction of the two oscillating dipoles.

The force constant for both *V*N dipoles is K_{VN} and is given by the relation

$$K_{VN} = m_N(\omega_{VN})^2, \tag{9}$$

where ω_{VN} is the LVM frequency of the *V*N defect at 663 cm^{-1}.[13]

The potential energy of the interacting dipole moments of relation (7) is given by[51]

$$U_{int} = \frac{1}{d^3_{N_A-N_B}}\left[\boldsymbol{p}_{t,A} \cdot \boldsymbol{p}_{t,B} - 3(\hat{\boldsymbol{n}} \cdot \boldsymbol{p}_{t,A})(\hat{\boldsymbol{n}} \cdot \boldsymbol{p}_{t,B})\right], \tag{10}$$

where $\hat{\boldsymbol{n}}$ is the unit vector along the direction that connects the two dipoles and $d_{N_A-N_B}$ = 4.81 Å is the distance between them. The motion of the two dipoles is described by the effective Hamiltonian

$$H = \frac{1}{2}m_N\dot{q}_A^2 + \frac{1}{2}m_N\dot{q}_B^2 + \frac{1}{2}K_{VN}q_A^2 + \frac{1}{2}K_{VN}q_B^2 + \lambda q_A q_B. \tag{11}$$

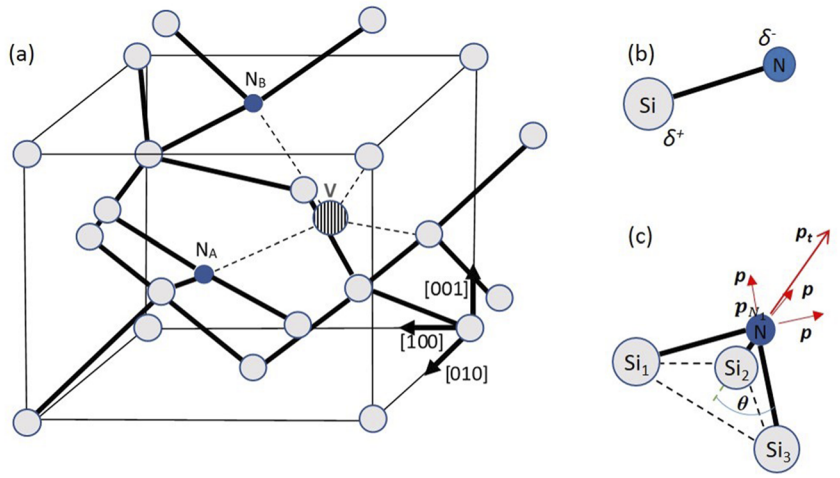

FIG. 7. (a) VN_2 configuration in Si. The striped circle denotes the vacant site while blue and light gray circles denote substitutional nitrogen and Si atoms, respectively. (b) The dipole moment $\boldsymbol{p}$ of the nitrogen atom due to the partial charges δ^- and δ^+ in nitrogen and silicon atoms, respectively. (c) The dipole moments $\boldsymbol{p}$ of the three individual N–Si bonds in the directions of these bonds and the total dipole moment $\boldsymbol{p}_t$ fixed on the nitrogen atom corresponding to the resultant of the three components of the individual dipole moments $\boldsymbol{p}$ in the direction passing through the nitrogen atom and being vertical to the base of the N–Si_3 pyramids (the Si–Si–Si plane). θ is half of the ∠Si–N–Si angle.

By comparing Eqs. (9) and (10), we obtain the q-independent part λ to be equal to $\lambda = 0.68 \mathrm{J/m^2}$. The Hamiltonian of Eq. (10) has two normal modes with frequencies

$$\omega_{VN_2} = \sqrt{\frac{1}{2}\left[\omega_{VN_A}^2 + \omega_{VN_B}^2 \pm \sqrt{(\omega_{VN_A} - \omega_{VN_B})^2 + \frac{4\lambda^2}{m_N^2}}\right]}. \quad (12)$$

By substituting $\omega_{VN_A} = \omega_{VN_B} = 663\ \mathrm{cm^{-1}}$ in Eq. (12), we find $\omega_{VN_2}^{(ant)} = 664\ \mathrm{cm^{-1}}$ and $\omega_{VN_2}^{(sym)} = 662\ \mathrm{cm^{-1}}$, corresponding to the antisymmetric normal mode (with the "+" sign inside the square root) and the symmetric one (with the "−" sign inside the square root), respectively. The modes $\omega_{VN_2}^{(ant)} = 664\ \mathrm{cm^{-1}}$ and $\omega_{VN_2}^{(sym)} = 662\ \mathrm{cm^{-1}}$ are remarkably close to the reported IR active A and A' modes at 672 and 669.1 $\mathrm{cm^{-1}}$, respectively, of the VN_2 defect.[13]

3. The divacancy-dinitrogen substitutional defect

Following the same procedure, we removed a further Si atom to create the second vacancy. Although we tried all the available positions for this second vacancy in the supercell, the most favorable position is with the two vacancies being close together. From a physical viewpoint, this can be explained because in the nearest neighbor site configuration, there is a reduction in the dangling bonds. Figure 8 shows the schematic representation of the lowest energy configuration of the V_2N_2 defect. The V_2N_2 defect consists of a VN_2 defect with the second vacant lattice site being the nearest neighbor to the first one. According to DFT outcomes, in V_2N_2 defect, all N–Si bonds and ∠Si–N–Si angles have the same values as in the case of VN_2 defect, and the distances between the two nitrogen atoms are equal in both defects ($d_{N_A-N_B} = 4.81$ Å).

As expected, after applying the dipole–dipole interaction method, this structural resemblance has resulted in the same values for the LVM frequencies of the V_2N_2 defect, that is, at 664 and 662 $\mathrm{cm^{-1}}$, as in the case of VN_2 defect. This is in agreement with the reported difference of only 1 $\mathrm{cm^{-1}}$ in the two calculated more intense LVM bands of the VN_2 and V_2N_2 defects at 675 and 676 $\mathrm{cm^{-1}}$, respectively.[16]

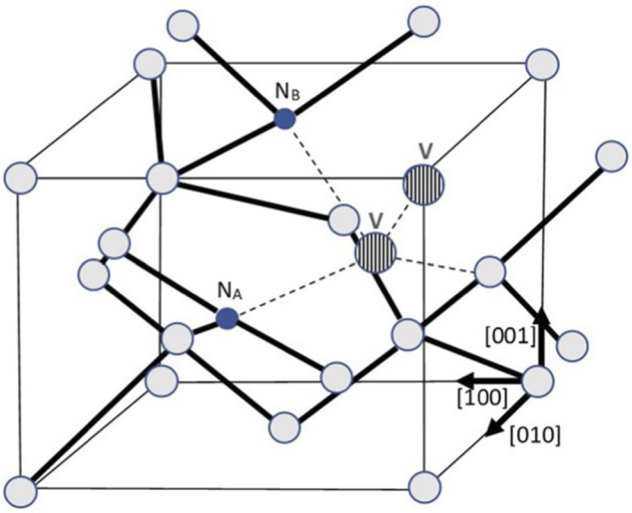

FIG. 8. V_2N_2 configuration in Si. Striped circles denote vacant sites while blue and light gray circles denote substitutional nitrogen and Si atoms, respectively. V_2N_2 consists of a VN_2 defect with the second vacancy being the nearest-neighbor to the first one.

IV. CONCLUSIONS

The aim of the present work was to study the vacancy-nitrogen defects in Si. DFT calculations were employed to calculate the most energetically favorable structures of the VN, VN_2, and V_2N_2 defects in Si. All the vacancy-nitrogen defects considered here are strongly bound, and therefore, they will readily form in a Si lattice provided that there is sufficient concentration of nitrogen and vacancies. A common feature is that the electrons are mainly localized on the N atoms. In these derived structures, we used the established dipole–dipole interaction method to calculate the LVM frequencies. For the VN defect, we calculate a frequency of 670 $\mathrm{cm^{-1}}$, in excellent agreement with previous experimental studies (663 and 668 $\mathrm{cm^{-1}}$).[13,16] Considering the VN_2 defect, we report here two frequencies at 664 and 662 $\mathrm{cm^{-1}}$, which are consistent with the 672 and 669.1 $\mathrm{cm^{-1}}$ calculated by Goss *et al.*[13] Notably, the structural resemblance of the VN_2 and V_2N_2 defects leads to the same frequencies.

SUPPLEMENTARY MATERIAL

See the supplementary material for the configurations (N-doped Si and N-doped Si with vacancy) obtained using full geometry optimization and fixed cell geometry optimization together with bond-lengths, bond-angles, and Bader chargers. Different configurations of NV, N_2V, and N_2V_2 defects are also provided.

ACKNOWLEDGMENTS

The High Performance Computing Centre at Imperial College London is acknowledged for providing computational facilities and support.

AUTHOR DECLARATIONS

Conflict of Interest

The authors have no conflicts to disclose.

DATA AVAILABILITY

The data that support the findings of this study are available from the corresponding author upon reasonable request.

REFERENCES

[1] M. D. McCluskey and A. Janotti, J. Appl. Phys. **127**, 190401 (2020).
[2] A. Chroneos, E. N. Sgourou, C. A. Londos, and U. Schwingenschlögl, Appl. Phys. Rev. **2**, 021306 (2015).
[3] K. Sumino, I. Yonenaga, M. Imai, and T. Abe, J. Appl. Phys. **54**, 5016 (1983).
[4] F. Shimura and R. S. Hockett, Appl. Phys. Lett. **48**, 224 (1986).

[5]H. Ishii, K. Oka, K. Motonami, T. Koyama, and J. Izumitani, Jpn J. Appl. Phys., Part 2 **35**, L1385 (1996).
[6]W. von Ammon, R. Hölzl, J. Virbulis, E. Dornberger, R. Schmolke, and D. Gräf, J. Cryst. Growth **226**, 19 (2001).
[7]D. Yang, R. Fan, L. Li, and D. Que, Appl. Phys. Lett. **68**, 487 (1996).
[8]E. N. Sgourou, T. Angeletos, A. Chroneos, and C. A. Londos, J. Mater. Sci.: Mater. Electron. **27**, 2054 (2016).
[9]C. Cui, X. Ma, and D. Yang, J. Appl. Phys. **104**, 123523 (2008).
[10]H. J. Stein, J. Electrochem. Soc. **132**, 668 (1985).
[11]A. Taguchi, H. Kageshima, and K. Wada, J. Appl. Phys. **97**, 053514 (2005).
[12]H. J. Stein, Appl. Phys. Lett. **47**, 1339 (1985).
[13]J. P. Goss, I. Hahm, R. Jones, P. R. Briddon, and S. Oberg, Phys. Rev. B **67**, 045206 (2003).
[14]N. Inoue and Y. Kawamura, J. Appl. Phys. **123**, 185701 (2018).
[15]A. Platonenko, F. S. Gentile, J. Maul, F. Pascale, E. A. Kotomin, and R. Dovesi, Mater. Today Commun. **21**, 100616 (2019).
[16]A. Platonenko, F. S. Gentile, F. Pascale, E. A. Kotomin, A. N. Ferrari, M. D'Amore, and R. Dovesi, Phys. Chem. Chem. Phys. **21**, 20939 (2019).
[17]G. Kresse and J. Furthmüller, Phys. Rev. B **54**, 11169 (1996).
[18]P. E. Blöchl, Phys. Rev. B **50**, 17953 (1994).
[19]H. J. Monkhorst and J. D. Pack, Phys. Rev. B **13**, 5188 (1976).
[20]J. P. Perdew, K. Burke, and M. Ernzerhof, Phys. Rev. Lett. **77**, 3865 (1996).
[21]W. H. Press, S. A. Teukolsky, W. T. Vetterling, and B. P. Flannery, *Numerical Recipes in C: The Art of Scientific Computing*, 2nd ed. (Cambridge University Press, 1992).
[22]J. Heyd, G. E. Scuseria, and M. Ernzerhof, J. Chem. Phys. **118**(18), 8207 (2003).
[23]G. Henkelman, A. Arnaldsson, and H. Jónsson, Comput. Mater. Sci. **36**, 354 (2006).
[24]M. Yu and D. R. Trinkle, "Accurate and efficient algorithm for Bader charge integration," J. Chem. Phys. **134**, 064111 (2011).
[25]S. Grimme, J. Antony, S. Ehrlich, and H. Krieg, J. Chem. Phys. **132**, 154104 (2010).
[26]B. N. Dutta, Phys. Status Solidi B **2**, 984 (1962).
[27]F. D. Murnaghan, Proc. Natl. Acad. Sci. U. S. A. **30**, 244 (1944).
[28]M. T. Yin and M. L. Cohen, Phys. Rev. B **26**, 5668 (1982).
[29]R. Zhachuk, Data Brief **28**, 104847 (2019).
[30]Y. Mo, H. Tang, A. Bansil, and J. Tao, AIP Adv. **8**, 095209 (2018).
[31]Y. J. Dappe, R. Oszwaldowski, P. Pou, J. Ortega, R. Pérez, and F. Flores, Phys. Rev. B **73**, 235124 (2006).
[32]W. Bludau, A. Onton, and W. Heinke, J. Appl. Phys. **45**, 1974 (1846).
[33]Z.-h. Yang, H. Peng, J. Sun, and J. P. Perdew, Phys. Rev. B **93**, 205205 (2016).
[34]M. Hu, Z. Wang, Y. Xu, J. Liang, J. Li, and X. Zhu, Phys. Chem. Chem. Phys. **20**, 26091 (2018).
[35]J. Heyd, J. E. Peralta, G. E. Scuseria, and R. L. Martin, J. Chem. Phys. **123**, 174101 (2005).
[36]H. Wang, A. Chroneos, C. A. Londos, E. N. Sgourou, and U. Schwingenschologl, Sci. Rep. **4**, 4909 (2014).
[37]A. L. Allred, J. Inorg. Nucl. Chem. **17**, 215–221 (1961).
[38]M. J. Puska, S. Pöykkö, M. Pesola, and R. M. Nieminen, Phys. Rev. B **58**(3), 1318 (1998).
[39]C. A. Londos, G. Antonaras, and A. Chroneos, J. Mater. Sci.: Mater. Electron. **24**, 4328–4331 (2013).
[40]A. N. Pandey, D. K. Sharma, and R. K. Goel, Spectrosc. Lett. **6**, 449–453 (1973).
[41]G. A. Ozin, J. Chem. Soc. A **1970**, 2307–2310.
[42]P. W. Atkins, *Physical Chemistry*, 5th ed. (Oxford University Press, 1994).
[43]C. Bastos and B. Leite, Orbital: Electron. J. Chem. **9**, 360–368 (2017).
[44]L. Pauling and L. J. Am, Chem. Soc. **54**, 3570 (1932).
[45]L. Pauling, *The Chemical Bond and the Structure of Molecules and Crystals: An Introduction to Modern Structural Chemistry*, 3rd ed. (Cornell University Press, New York, 1960).
[46]L. C. Allen, J. Am. Chem. Soc. **111**, 9003–9014 (1989).
[47]N. V. Sarlis, C. A. Londos, and L. G. Fytros, J. Appl. Phys. **81**, 1645 (1997).
[48]M. S. Potsidi and C. A. Londos, J. Appl. Phys. **100**, 033523 (2006).
[49]M. S. Potsidi, N. Kuganathan, S.-R. G. Christopoulos, A. Chroneos, T. Angeletos, N. V. Sarlis, and C. A. Londos, Crystals **10**, 1005 (2020).
[50]M. S. Potsidi, N. Kuganathan, A. Chroneos, S.-R. G. Christopoulos, T. Angeletos, N. V. Sarlis, and C. A. Londos, Mater. Sci. Semicond. Process. **127**, 105661 (2021).
[51]J. Jackson, *Classical Electrodynamics* (Wiley, New York, 1975), p. 136.